metals

MDPI

Article

Microstructures and High Temperature Tensile Behaviours of Laser Powder Bed Fusion Fabricated Al-Mn-Sc Alloy

Yuqing Yan, Chengqi Lu, Zhenyu Chen, Yuhao Zhuo, Chuanyang Wang * and Qingbo Jia *

School of Mechanical and Electrical Engineering, Soochow University, Suzhou 215131, China
* Correspondence: cywang@suda.edu.cn (C.W.); qbjia@suda.edu.cn (Q.J.)

Abstract: The introduction of Sc/Zr inoculates to aluminium (Al) alloys for laser powder bed fusion (LPBF) provides numerous benefits, including laser processability improvement, solidification microstructure control and mechanical property enhancement. Though great efforts have been put into tailoring the microstructure and room temperature mechanical properties via process parameter optimisations, the potential roles of Sc/Zr inoculate modified Al alloys for high-temperature applications were still underexplored. In this study, the microstructural stability and the elevated temperature tensile behaviours of LPBF-processed Al-Mn-Sc alloy were systematically evaluated. The alloy demonstrated high microstructural stability after both heat treatment and high-temperature tensile testing for up to 573 K. The applied tensile testing temperature and strain rate played significant influences on the elevated temperature tensile properties and deformation behaviours. Unusual intermediate temperature embrittlement (also known as ductility dip) and yield drop behaviours were observed under certain testing temperature and strain rate regimes, and the underlying deformation mechanisms were elucidated in detail. The present study is expected to shed light on future high-performance, high-temperature Al alloy development for the LPBF process.

Keywords: laser powder bed fusion; aluminium alloys; scandium; high temperature tensile; ductility dip

check for updates

Citation: Yan, Y.; Lu, C.; Chen, Z.; Zhuo, Y.; Wang, C.; Jia, Q. Microstructures and High Temperature Tensile Behaviours of Laser Powder Bed Fusion Fabricated Al-Mn-Sc Alloy. *Metals* **2023**, *13*, 788. https://doi.org/10.3390/met13040788

Academic Editor: Antonello Astarita

Received: 24 March 2023
Revised: 10 April 2023
Accepted: 14 April 2023
Published: 17 April 2023

Copyright: © 2023 by the authors. Licensee MDPI, Basel, Switzerland. This article is an open access article distributed under the terms and conditions of the Creative Commons Attribution (CC BY) license (https://creativecommons.org/licenses/by/4.0/).

1. Introduction

Laser powder bed fusion (LPBF), as one of the most widely studied additive manufacturing (AM) techniques, offers the unique capability of fabricating geometrically complex components [1]. It gained enormous interest in the past decade and has now become a successive alternative to conventional manufacturing routes due to its very limited tooling cost and material wastage [2]. Moreover, the ultrafast cooling rate and the repeated thermal cycling metallurgical features endow distinctive non-equilibrium microstructures and elegant mechanical properties of the fabricated parts [3–5]. Such metallurgical features distinguish the LPBF process from traditional ingot processing, wherein relatively coarse equilibrium microstructures and mediocre mechanical properties are obtained. To date, high-performance components have been successfully fabricated by LPBF in the fields of aerospace, automotive, medical, nuclear, etc. [6].

Apart from the above inherent advantages of the LPBF process, lacking available materials limited its rapid development towards extensive applications. Specifically, the majority of the existing commercial alloys cannot be reliably processed by LPBF due to the generated severe metallurgical defects, especially the solidification cracks [7]. This is mainly because the highly localised high-energy laser beam created an unusual solidification environment of extremely high thermal gradient and ultrafast cooling rate within the hundreds of micron-sized molten pools, triggering the long columnar grain growth and the huge thermal stress generation within the fabricated parts. At the later solidification stage, with the volumetric solidification shrinkage and thermal contraction of the trapped liquid along the columnar grain boundary areas, intolerable solidification cracks occur due to the breakdown of the solid-liquid interface in the intergranular channels. Thus, there

has now been a growing realisation of developing new high-performance alloys that are amenable to the LPBF process, with the final goal of broadening the property window of the processed parts [8].

Among all the studied metallic materials for the LPBF process, aluminium (Al) alloys have suffered the most due to the frequently observed solidification cracks, especially for the LPBF-fabricated high-strength wrought Al alloys [9–11]. Though great efforts have been made to optimise process parameters to improve the alloy processability; however, the solidification cracks still cannot be avoided effectively. Recently, it was found that grain refinement can significantly improve the alloy processability and mechanical properties of the LPBF-fabricated Al alloys [12–14]. Either the extrinsically incorporated or the in situ formed inoculates can be worked as effective nucleation sites, leading to the remarkable grain refinement to accommodate the residual strains and avoid the solidification cracks. Benefiting from the introduced inoculates, grain refinement has now become mainstream research for high-strength Al alloy development for the LPBF process.

On the other hand, the rapid solidification nature of the LPBF process enables large amounts of slow diffusing transition metals and/or rare earth elements to be placed into a solid solution, which opens up a new avenue for high-performance Al alloy design for the LPBF process. As a typical example, the introduction of Sc/Zr inoculates into Al alloys provides great benefits for LPBF processability improvement, solidification microstructure control as well as mechanical property enhancement, mainly due to the precipitation of the $L1_2$ structured trialuminides [15–18]. The Sc/Zr contained Al alloys have been widely used in aerospace and automobile fields for structural components manufacturing [19]. The minimal lattice misfit between the primary Al_3(Sc, Zr) particles and the Al matrix enabled its effective nucleation site roles to promote grain refinement [20,21]. Moreover, its unique distribution resulted from the local solidification conditions promoted a heterogeneous grain structure with an alternative growth of the relatively coarse columnar grains and the ultrafine equiaxed grains, which markedly alleviated the hot cracking susceptibility of LPBF-fabricated Al alloys [22]. Upon further post-heat treatment, the decomposition of the supersaturated Sc/Zr solutes formed large amounts of nano-sized Al_3(Sc, Zr) precipitates, which significantly enhanced the mechanical properties of LPBF-fabricated Al alloys. So far, dedicated research efforts have been put to understand the multiple effects of Sc/Zr inoculates modified Al alloys after LPBF fabrication [23–25]; the elevated temperature mechanical properties of such alloys were still underexplored, though the formed Al_3(Sc, Zr) precipitates possessed good thermal stability and high-temperature strengthening effects. Moreover, how the novel heterogeneous grain structure behaves under elevated temperature tensile deformation conditions also remains unclear.

In this study, the microstructure and elevated temperature tensile performance of LPBF-processed Al-Mn-Sc alloy were systematically investigated. In particular, we evaluated the effect of tensile testing conditions (including temperature and tensile strain rate) on the microstructural stability and deformation behaviours of LPBF-fabricated Al-Mn-Sc alloy due to its possible application under a dynamic load environment. The relationship between the microstructure, the tensile deformation condition and the elevated temperature mechanical properties were established, and the underlying strengthening mechanisms were elucidated through various characterisation techniques. The present study provides a fundamental understanding of the elevated temperature tensile behaviours of Sc/Zr inoculates modified Al alloys after LPBF fabrication, with the ultimate goal of contributing to future high-temperature, high-performance Al alloy development for the LPBF process.

2. Materials and Methods

2.1. Sample Preparation

The gas-atomised powders were fabricated from cast ingots through a vacuum induction gas atomisation (VIGA) process under an argon environment. The powder morphology and its typical size distribution are shown in Figure 1. Spherical-shaped powders in the 20–53 μm size range were sieved for SLM fabrication using a commercial EOS M290 ma-

chine that coupled with a 400-W fibre laser at a constant laser spot size of 100 µm. Cubic samples (15 × 15 × 15 mm^3) used for microstructural observations were built with a laser power of 370 W, scan speed of 1000 mm/s, hatch distance of 0.1 mm, and layer thickness of 0.04 mm. The machine default strip scan strategy with a fixed strip width of 7 mm and a scan direction rotation of 67° between consecutive layers was applied for all the processed samples. The chemical compositions of the fabricated samples were determined to be Al-4.46Mn-1.09Mg-0.8Sc-0.64Zr-0.08Fe-0.06Si (in wt%) by inductively coupled plasma atomic emission spectroscopy (ICP-AES). The built samples were then subjected to a salt bath for post ageing treatment at 300 °C to achieve further precipitation strengthening.

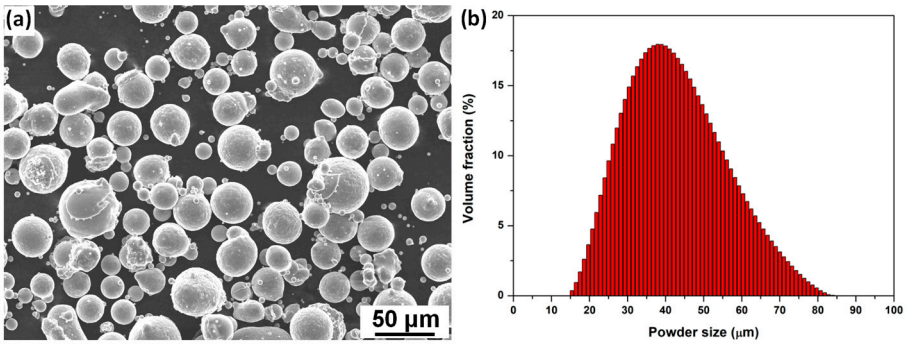

Figure 1. The gas atomised powder morphology (**a**) and its typical size distribution (**b**).

2.2. Microstructure Investigation

X-ray diffraction (XRD) for phase identification was performed on a Bruker D8 Discover diffractometer (Bruker, Billerica, MA, USA)with Cu-Kα (λ = 0.15046 nm) radiation operating at 42 kV and 100 mA, with a selected scanning 2θ range of 30–90° and each step of 0.02°. A Zeiss Gemini 300 scanning electron microscope (SEM) (Zeiss, Germany), equipped with an Oxford electron backscattered diffraction (EBSD) detector, was used for microstructure analysis. Samples for EBSD investigations were all electropolished with an electrolyte solution composed of 10 vol.% perchloric acid and 90 vol.% ethanol. Bright-field (BF) transmission electron microscopy (TEM) and scanning transmission electron microscopy (STEM) images were recorded on an FEI Tecnai G2 F20 TEM microscope (Thermo Fisher, Waltham, MA, USA) operating at 200 kV. Samples for transmission electron microscope (TEM) studies were firstly ground into 100 um thick and then electropolished by a Tenupol twin jet polishing system (Struers, Denmark) in a solution of 67 vol.% methanol and 33 vol.% nitric acid at 12.8 V and −30 °C.

2.3. Mechanical Property Testing

Samples used for tensile testing were firstly built into a hexagonal prism shape with dimensions of 70 mm in length and 10 mm in diagonal. The sample was then mechanically machined by turning them into cylindrical tensile samples with a gauge length of 26 mm and a diameter of 4 mm, and the sample clip areas were also screw-threaded into the standard size of M8 (Figure 2). Uniaxial tensile tests were all conducted on a Shimadzu AG-IC 100KN machine (Shimadzu, Japan) equipped with a heating furnace and two types of epsilon extensometers for respective room temperature and elevated temperature strain measurements. The applied tensile testing samples were all built in the horizontal direction (parallel to the powder bed platform), and each testing condition was repeated three times to confirm the data's repeatability. Room temperature tensile properties were evaluated at a constant strain rate of 3 × 10^{-4} s^{-1} according to the ASTM E8 standard. For the elevated temperature tensile testing, the tensile samples were performed at a strain rate range of approximately 10^{-5}–10^{-2} s^{-1} and a temperature range of 423–573 K according to the ASTM E21 standard. All the samples used for elevated temperature tensile evaluation were soaked at the predefined testing temperatures for at least 20 min before loading.

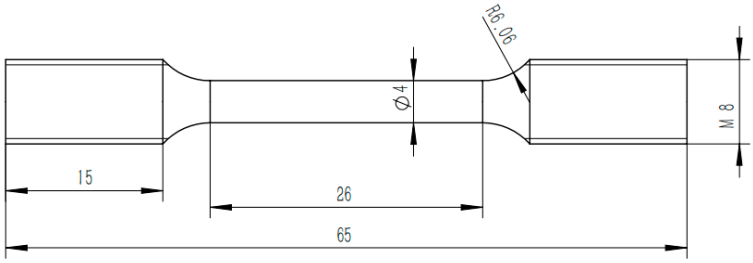

Figure 2. The sample geometry was used for both room and elevated temperature tensile testing.

3. Results

3.1. Microstructure in the as Built Condition

Figure 3 shows the molten pool features and the corresponding XRD spectrum of the as-built samples along both the vertical (perpendicular to the powder bed platform) and the horizontal (parallel to the powder bed platform) directions. Irregular molten pool distribution behaviours resulting from the rotational scan strategy were obtained in the sample's vertical direction (Figure 3a). The distinguished colour contrast between the boundary and the centre areas within individual molten pools was observed. The inserted higher magnification images revealed that this is mainly due to the different etching effects of the formed heterogeneous grain structures, i.e., relatively coarse columnar grains within the molten pool centre areas and ultrafine equiaxed grains along the molten pool boundaries. On the horizontal plane of the built sample, elliptical-typed scanning track features with heterogeneous grain distributions were captured, with ultrafine equiaxed grains along the scanning track boundary and the relatively coarse equiaxed grains within the track centre areas (Figure 3b). The respective XRD patterns from both horizontal and vertical directions revealed that the diffraction peaks mainly correspond to the Al matrix, and no other obvious phases can be identified (Figure 3c,d). In comparison with the vertical direction, the higher diffraction peak intensity of the $(200)_{Al}$ peak was captured on the horizontal plane, indicating more grains shared the same preference along such crystal orientations. Nevertheless, a previous study has confirmed that the alloy generally exhibited negligible anisotropic mechanical properties [26].

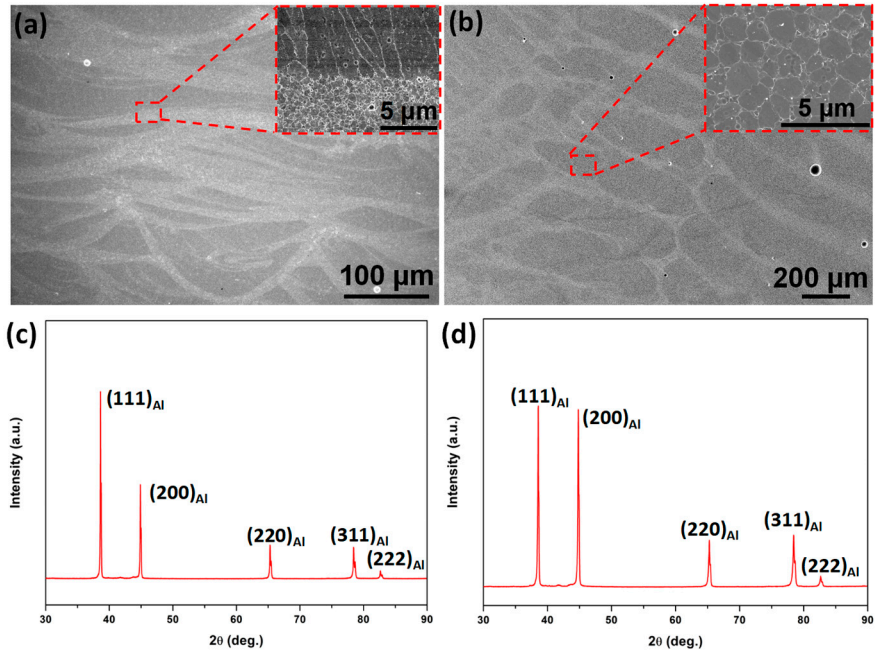

Figure 3. SEM micrographs showing microstructure along (**a**) vertical and (**b**) horizontal planes of the LPBF-fabricated Al-Mn-Sc alloy samples; (**c**,**d**) are the corresponding XRD patterns of (**a**,**b**).

Higher magnification TEM micrographs provided more detailed microstructures within the columnar grain and the equiaxed grain regions (Figure 4). Primary Al_6Mn particles are observed within the columnar grain regions, while TEM sample tilting revealed that such particles are typically aligned along the grain and subgrain boundaries. This suggested that the primary Al_6Mn particles were mainly formed due to solute rejection from the liquid front and subsequently nucleated along the energy-favoured grain and subgrain boundaries [27]. Further, primary Al_3(Sc, Zr) particles that facilitated the formation of heterogeneous grain structures are located mainly within the equiaxed grain areas due to the local unique solidification environment. Herein, previous studies proposed that the formation mechanisms of such primary Al_3(Sc, Zr) particles can be attributed to either the remelting theory of low melt over-heating or the solute-trapping theory of the local low solidification rate along the molten pool boundaries [28,29]. The layer-by-layer building nature of the LPBF thus triggered the formation of heterogeneous grain structures along the sample building direction.

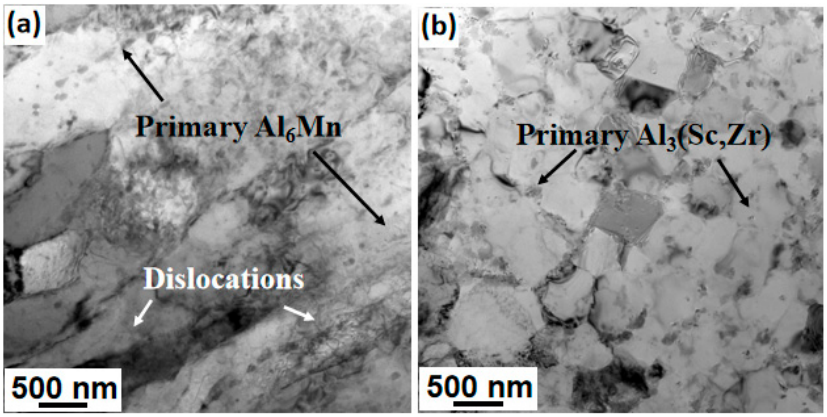

Figure 4. TEM images showing the Al-Mn-Sc alloy microstructures in (**a**) columnar grain regions and (**b**) equiaxed grain regions in the as-fabricated condition.

3.2. Microstructure after Heat Treatment

The fabricated samples were then subjected to post-heat treatment at 300 °C for 5 h to achieve further precipitation hardening [24]. Figure 5a shows the EBSD grain structure of the heat-treated sample, wherein the heterogeneous grain structure was successfully maintained. The statistical results showed that grains with a size below 2 μm dominated almost half of the investigated sample areas, with the average grain size determined to be 0.88 ± 0.8 μm (Figure 5b). The band contrast map shows a sharp interface between the heterogeneous grain structures, while the majority of the grains are separated by high-angle grain boundaries with a misorientation angle of adjacent grains larger than 15° (Figure 5c). Moreover, the average kernel misorientation (KAM) map reflected that some strain energy was still stored in the columnar grain regions, suggesting no obvious grain recrystallisation occurred during the post-heat treatment process (Figure 5d). The grain structure comparison between the fabricated condition (can be found in Ref. [26]) and the above heat treatment condition also supports the above conclusion. The insignificant recrystallisation behaviour can be attributed to the good thermal stability and grain growth inhibiting capabilities of the formed primary Al_6Mn and Al_3(Sc, Zr) particles, which effectively hindered the alloy grain growth and recrystallisation [30]. Nevertheless, it has been demonstrated that the majority of the residual stresses resulting from the thermo-mechanical cycles of the LPBF process can be relieved after the above heat treatment [26].

BF STEM images further confirmed that the heterogeneous grain structures and the generated primary particles maintained their original size and shape after heat treatment (Figure 6). Furthermore, a high-resolution TEM image showed the precipitation of the secondary Al_3(Sc, Zr) precipitates, with the size of the precipitates measuring about 2–6 nm (Figure 6c). The inserted fast Fourier transformation (FFT) image revealed the $L1_2$ superlat-

tice reflection from the secondary Al_3(Sc, Zr) precipitates. Moreover, the secondary Al_3(Sc, Zr) precipitates and the Al matrix exhibited high coherency with the absence of interface strain features. The phase contrast was also appreciated by the line profile taken along the Al matrix (line AB) and the Al_3(Sc, Zr) precipitates (line CD), wherein minimal lattice parameter mismatch between the above two phases was determined, further confirming the high coherency between the precipitates and the Al matrix (Figure 6d).

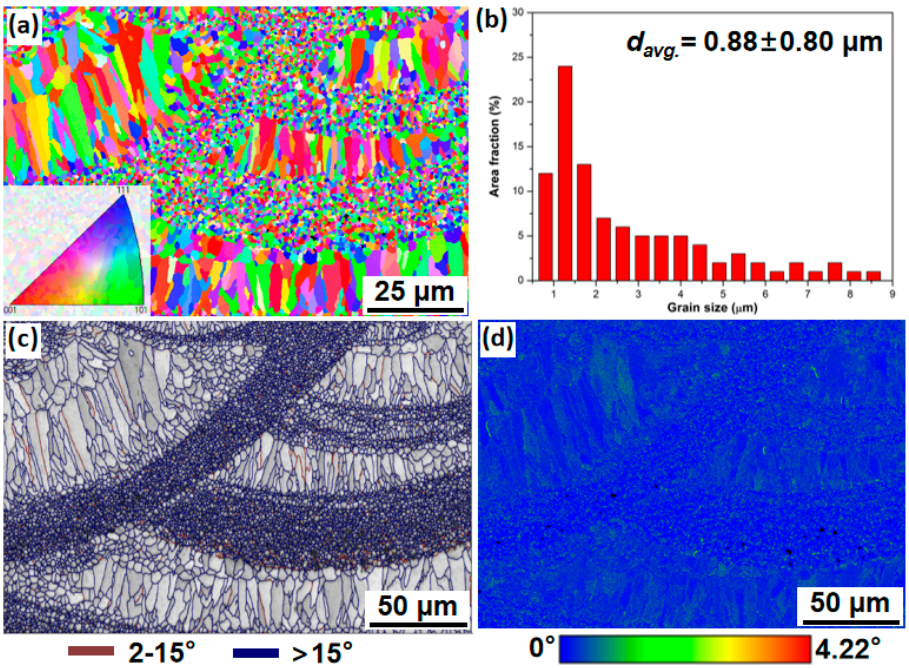

Figure 5. EBSD images showing (**a**) heterogeneous grain structure, (**b**) grain size distribution, (**c**) band contrast map and (**d**) KAM mapping of the heat-treated Al-Mn-Sc alloy.

3.3. Mechanical Property

The room temperature mechanical property of the LPBF-fabricated Al-Mn-Sc alloy was evaluated by tensile testing. Figure 7a shows the typical engineering stress-strain curves in both the as-fabricated and heat-treated conditions. The alloy achieved a yield strength of 427 ± 11 MPa and a total elongation of 21.7 ± 2% in the as-fabricated condition, compared to 572 ± 4 MPa and 16.5 ± 2% after ageing treatment at 300 °C for 5 h, respectively. Moreover, the studied Al-Mn-Sc alloy exhibited discontinuous yielding and a low degree of work hardening behaviours, especially in the heat-treated condition. The fracture morphology studies revealed that the alloy generally exhibited a ductile fracture in the as-fabricated condition, as evidenced by the formed small dimples (Figure 7b). In this case, molten pool tracks resulting from material tensile extraction during testing were observed. The fracture surface becomes more flattened with features of small dimples in the fine equiaxed grain areas and the cleavage fracture surface in the columnar grain regions, suggesting a brittle and ductile mixed fracture mode in the heat-treated condition (Figure 7c). Closer inspection revealed that tensile cracks propagated along the heterogeneous grain structure interface, indicating a strong stress concentration effect around the molten pool boundary areas.

The tensile properties of heat-treated Al-Mn-Sc alloy samples were then evaluated at elevated temperatures under various strain rates (Figure 8). Overall, the strengthening and deformation behaviours varied significantly with the applied testing temperatures and strain rates. To gain an intuitive understanding of the alloy tensile property variance at elevated temperatures, the alloy yield strength, ductility, ultimate tensile strength and Young's modulus were summarised as a function of testing temperatures and strain rates in Figure 9, respectively. In general, the yield strength and ultimate tensile strength decreased monotonically with the increment of the tensile testing temperatures, while it increased

gradually with the increment of the applied strain rate (Figure 9a,c). The fracture strain, however, exhibited an unexpected non-monotonically changing behaviour (Figure 9b). A ductility dip behaviour occurred at tensile testing temperatures of 473 K and 523 K under the corresponding strain rate of 10^{-5}–10^{-3} s^{-1}. By further increasing the applied strain rate to 10^{-2} s^{-1}, similar fracture strains were captured at the tensile testing temperature range of 423–523 K though it decreased to about 8% at 573 K. Further, the alloy Young's modulus exhibited fluctuations with the applied high-temperature tensile testing conditions, possibly due to testing setup variance (Figure 9d).

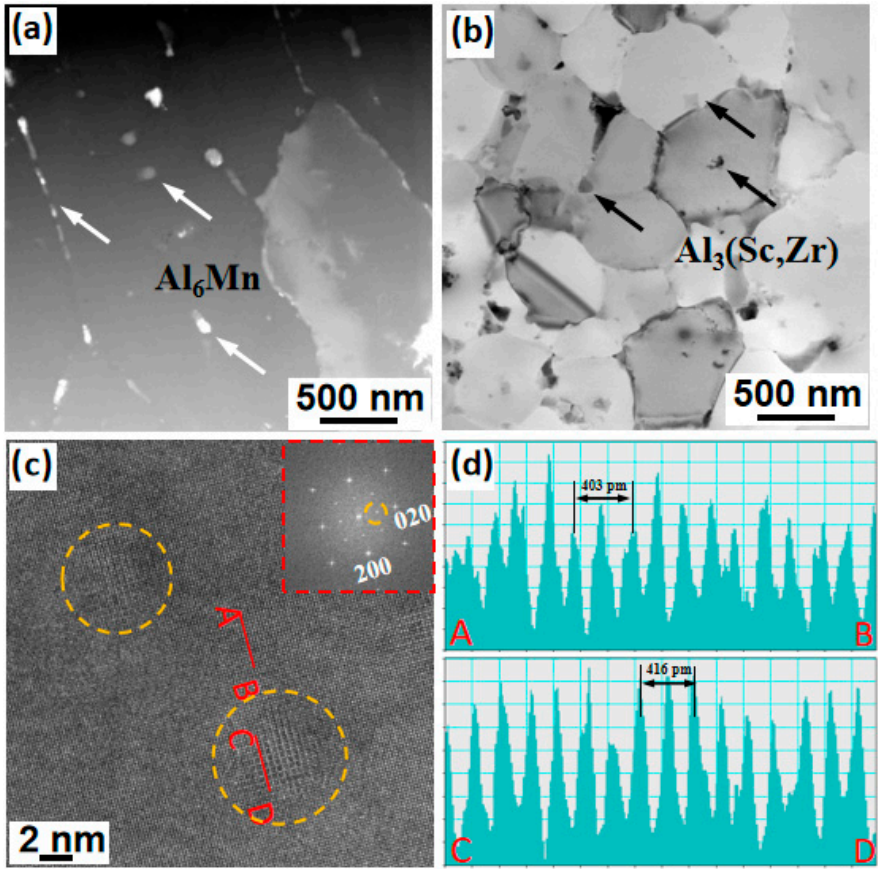

Figure 6. BF STEM images showing (**a**) the primary Al_6Mn particles in columnar grains and (**b**) primary $Al_3(Sc, Zr)$ particles in equiaxed grains of the heat-treated Al-Mn-Sc alloy; (**c**) HRTEM images showing the secondary $Al_3(Sc, Zr)$ precipitates and (**d**) line profiles taken along AB and CD in (**c**).

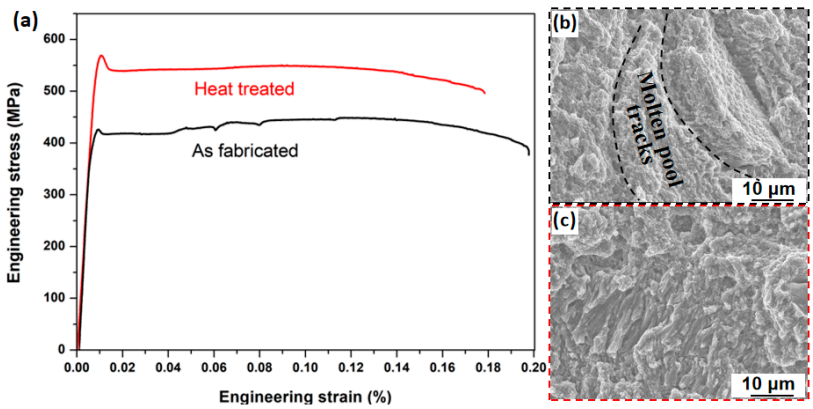

Figure 7. (**a**) Engineering stress-strain curves in both as-fabricated and heat-treated conditions, (**b**) fracture morphology in the as-fabricated condition and (**c**) fracture surface in the heat-treated condition.

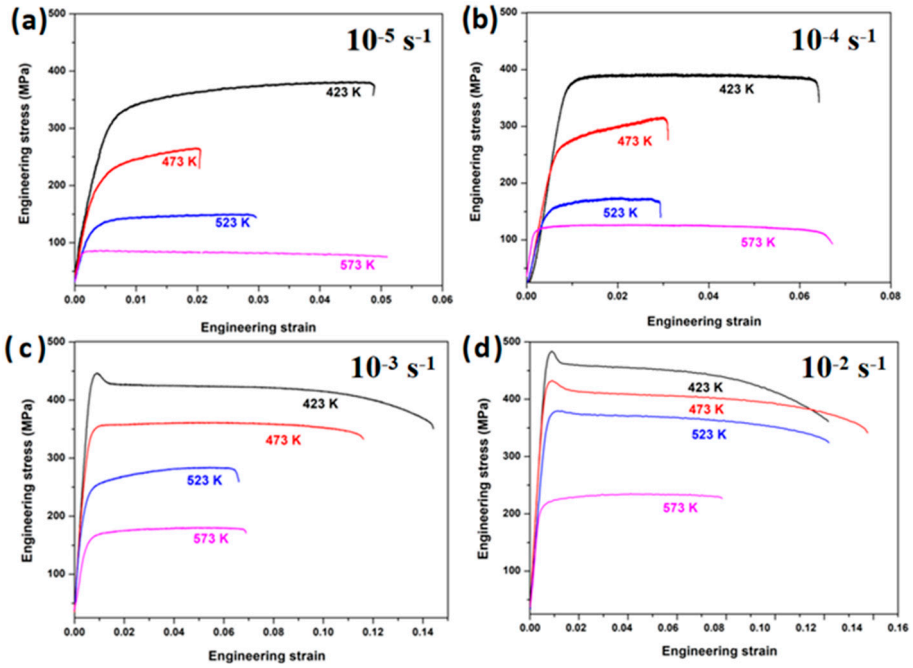

Figure 8. Representative elevated temperature engineering stress-strain curves of Al-Mn-Sc alloy at various temperatures and strain rates of (**a**) 10^{-5} s^{-1}, (**b**)10^{-4} s^{-1}, (**c**) 10^{-3} s^{-1} and (**d**) 10^{-2} s^{-1}.

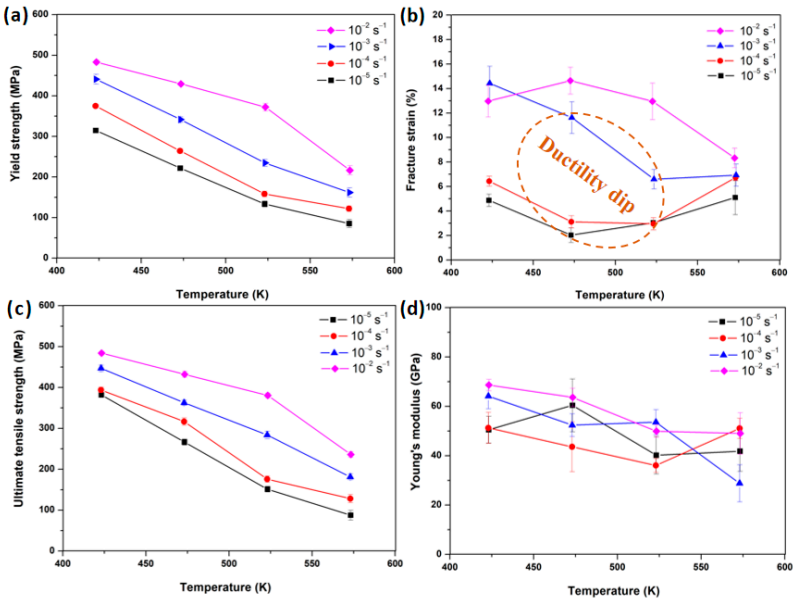

Figure 9. The summarised (**a**) yield strength, (**b**) fracture strain, (**c**) ultimate tensile strength and (**d**) Young's modulus as a function of testing temperatures and strain rates. Typical errors (variation from the mean) for yield strength/ultimate tensile strength and fracture strain are within ±10 MPa and ±2%, respectively.

Figure 10 shows the representative fracture surface morphology after elevated temperature tensile testing of the heat-treated Al-Mn-Sc alloy. As can be seen from Figure 10a, similar to the room temperature fracture surface in the heat-treated condition, the columnar-equiaxed grain-type features were observed on the fracture surface when tested at 523 K and 10^{-4} s^{-1}. However, a higher magnification image revealed that fracture dimples were observed in the columnar grain region, indicating a ductile fracture mode transition occurred upon testing at elevated temperature (Figure 10b). By increasing the applied testing strain rate to 10^{-2} s^{-1}, the fractured surface became more rugged, with dimples

dominating the whole cross-section (Figure 10c,d), which corresponds well with the significantly increased ductility in Figure 8. On the other hand, molten pool tracks reflected by the stair-type fracture surface were captured at 573 K with a tensile strain rate of 10^{-4} s^{-1} (Figure 10e). Compared with the sample tested at 523 K, fewer columnar grain areas can be observed on the fracture surface, while the columnar grain edges also become less sharp. Closer inspection revealed the granular characteristics on the fracture surface, which might be resulted from alloy oxidation during elevated temperature tensile testing (Figure 10f).

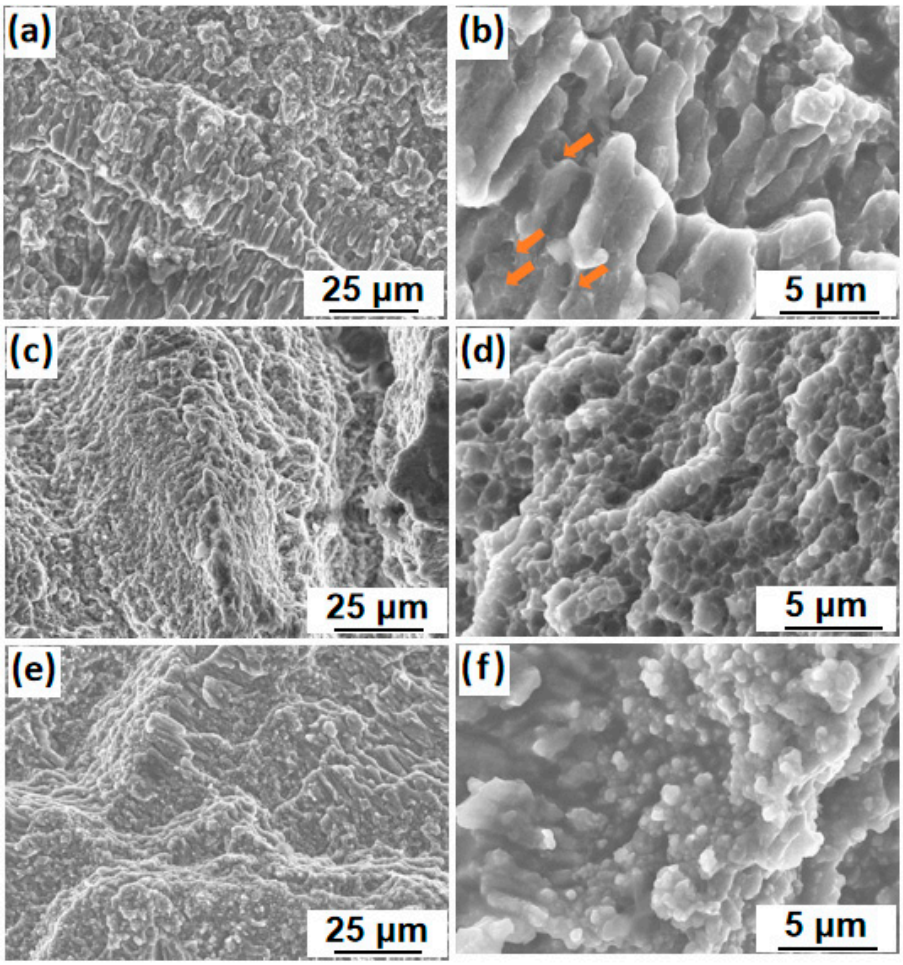

Figure 10. The fracture surface morphology of samples tested at (**a**) 523 K, 10^{-4} s^{-1}, (**c**) 523 K, 10^{-2} s^{-1} and (**e**) 573 K, 10^{-4} s^{-1}, (**b**,**d**,**f**) are higher magnification images of (**a**,**c**,**e**), respectively.

4. Discussion

4.1. Microstructural Stability and High-Temperature Strengthening Mechanisms

The ambient temperature strengthening mechanisms of the LPBF-fabricated Al alloys have been studied extensively, in which grain boundary strengthening, solid solution strengthening, and precipitation hardening were cited as the main strengthening mechanisms to the alloy yield strength at room temperature [24]. However, to maintain the above strengthening effects at elevated temperatures, grain growth, precipitation of non-hardening phases as well as precipitate coarsening have to be inhibited when exposed to the straining process under elevated temperatures. A previous study confirmed that no obvious grain recrystallisation and/or grain growth was found after ageing treatment even up to 723 K for 6 h, thanks to the formed thermally stable grain growth inhibitors of primary Al_6Mn and Al_3(Sc, Zr) particles [30]. In the present study, as seen in Figure 11, the grain size and its distributions were well-preserved after tensile testing at a strain rate of 10^{-3} s^{-1} and testing temperatures of both 473 K and 573 K. Further TEM investigations

revealed that the particles generally maintained their original size, suggesting no significant solute decomposition and/or precipitates coarsening after the above-elevated temperature tensile evaluation (Figure 12).

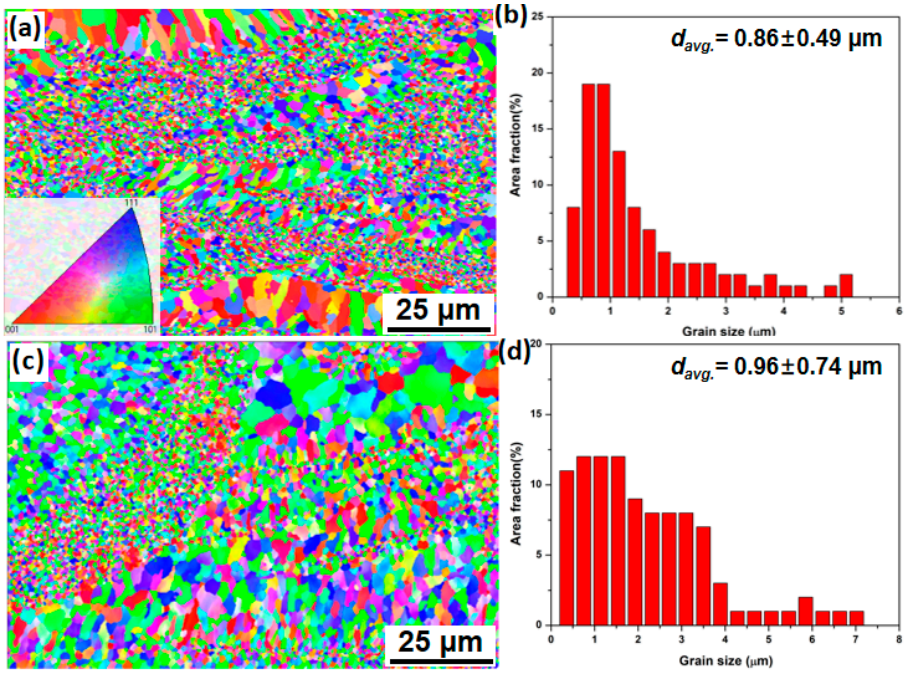

Figure 11. EBSD images showing (**a**,**c**) heterogeneous grain structures and (**b**,**d**) grain size distributions of samples after high-temperature tensile testing. Samples are tested with testing temperatures of (**a**,**b**) 473 K and (**c**,**d**) 573 K at a constant testing strain rate of 10^{-3} s^{-1}.

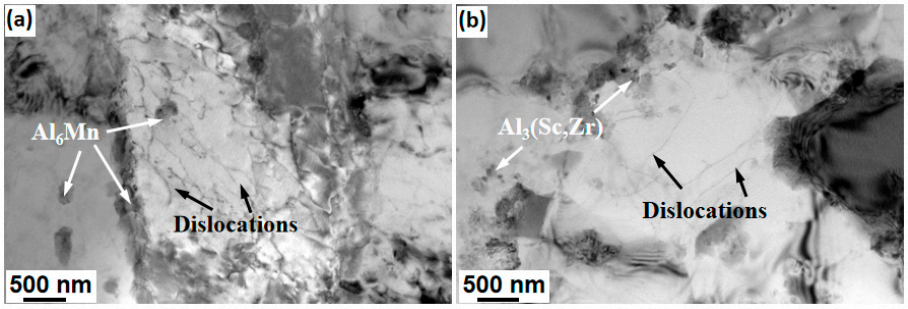

Figure 12. TEM images showing microstructure in (**a**) columnar grain region and (**b**) equiaxed grain region after tensile testing at 573 K, 10^{-3} s^{-1}.

With the increment of the applied tensile testing temperatures, the alloy yield strength exhibited a monotonic decrement (Figure 9). Though the above microstructural features are still expected to be the dominant strengthening contributors, the strengthening effects are correspondingly lowered at elevated temperatures. For solid solution strengthening, the strengthening contribution stems from the changes in lattice parameters caused by solute addition, where the strong interaction of dislocation's stress field with the lattice misfit strain tensor elevated the alloy strength. With the increment of tensile testing temperatures, dislocations can now easily unpin and escape from the local energy state and glide more favourably on the slip plane due to the enhanced atom vibration and the reduced energy field around both the dislocation cores and the solute atoms. For precipitates that are sufficiently small and coherent with matrix, which is the current case of Al_3(Sc, Zr) precipitates, it is generally believed shearing mechanisms dominated the strengthening effect from precipitates. The modulus mismatch between the dislocations

and the shearable precipitates is taken as the major strengthening contribution at room temperature [24]. However, with the assistance of the enhanced thermal vibration of atoms at high temperatures, dislocations overcome both the alloy matrix (the Peierls barrier) and the precipitates become easier as the atomic bonding and the resultant matrix shear modulus normally decreases as a function of heating temperature. Moreover, the atom diffusion behaviours within the precipitates and the matrix can be significantly improved under the applied thermal energy and tensile stress, further decreasing the alloy yield strength by favouring dislocation passing the above obstacles. Similarly, the grain boundary strengthening effect by impeding dislocation movement can also be dramatically weakened with the increment of the applied testing temperatures, as dislocation annihilation is significantly enhanced along the grain boundary areas.

Further, the alloy yield strength is also positively associated with the testing strain rate, resulting in a temperature and strain-rate-dependent plastic deformation behaviour, namely creep. According to the creep deformation theory, the alloy yield strength (σ_y) can be essentially expressed as [31]:

$$\sigma_y = E(\varepsilon/\varepsilon_0)^{\frac{1}{n}} \exp(Q/nRT) \quad (1)$$

where E is Young's modulus, ε is the applied strain rate, ε_0 is a material constant, n is the stress exponent, Q is the activation energy for lattice diffusion, R is the universal gas constant, and T is the absolute temperature. To verify the applicability of the above equation in the current study, a simple natural logarithm calculation of σ_y as a function of $1/T$ was plotted in Figure 13. Apart from the high strain rate at 10^{-2} s^{-1}, good linear fitting was obtained, confirming the dominated creep deformation mechanisms under the applied tensile testing temperatures and strain rates. Moreover, it also can be found that the slope of the fitted curves is basically similar, indicating the relatively consistent activation energy for the applied testing conditions. Thus, as expected from Equation (1), the yield stress decreases with the increment of testing temperature or decrement of strain rate.

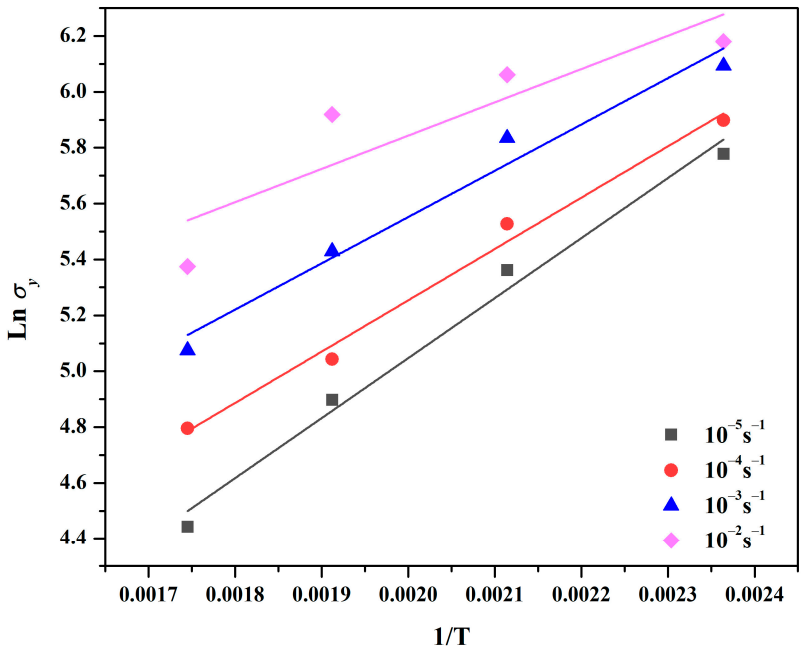

Figure 13. The natural logarithm fitting of yield strength as a function of $1/T$ of samples evaluated at different testing temperatures and strain rates.

4.2. Elevated Temperature Ductility Behaviours

4.2.1. Ductility Dip Phenomenon

The tested Al-Mn-Sc alloy exhibited an unexpected ductility dip phenomenon at an intermediate temperature range of 475–523 K and the corresponding strain rate of 10^{-5}–10^{-3} s^{-1}, which can be essentially called "intermediate temperature embrittlement" or "ductility dip cracking". Such phenomenon has been previously reported in many alloy systems that were made by conventional manufacturing routes, including Al alloys, Ni alloys, Cu alloys and steels [32–36]. The deformation and failure mechanisms were mainly attributed to the intergranular failure by crack initiation from grain boundary precipitates, grain boundary sliding, environmental degradation of grain boundaries, and/or grain boundary segregation. Another form of intermediate temperature embrittlement is due to reheat cracking and/or stress relaxation cracking in the welded stainless steels [37]. However, as discussed above, the microstructural features possessed outstanding thermal stability even after tensile testing at 573 K with a strain rate of 10^{-3} s^{-1}. Moreover, it has been confirmed that the majority of the residual stress can be relieved without the occurrence of cracks after the applied post-heat treatment [26]. Thus, the above failure mechanisms cannot fully explain the ductility dip phenomenon observed in LPBF-processed Al-Mn-Sc alloy. Recently, Bahl et al. reported a new post-uniform elongation dip phenomenon in an LPBF-fabricated Al-9Cu-6Ce alloy, wherein the root cause was associated with the strain rate sensitivity (SRS) reduction caused by the formed heterogeneous grain structure [38]. Nevertheless, the ductility dip behaviour in the current study cannot be directly attributed to the above SRS reduction mechanism, as no obvious post-uniform elongation dip behaviour can be identified.

In order to investigate the underlying deformation and fracture mechanisms of the present ductility dip phenomenon, the fractured sample region was sectioned and subjected to a microstructure study. SEM investigation revealed that no obvious voids and/or cracks were captured near the fractured region, indicating a non-site-specific failure initiation mode. EBSD was then applied to evaluate the plastic strain distribution behaviours near the fractured sample edges (Figure 14), using samples tested at 523 K with respective testing strain rates of 10^{-4} s^{-1} and 10^{-2} s^{-1} for comparison purposes. Herein, the 10^{-4} s^{-1} sample represents the alloy with intermediate temperature embrittlement, while the latter possessed higher tensile ductility. Both samples exhibited no obvious grain boundary sliding or dynamic recrystallisation after elevated temperature tensile evaluation (Figure 14a,b). The corresponding KAM maps revealed the high strain energy and the resultant high dislocation density concentrated along the heterogeneous grain structure interface of the sample tested at a lower strain rate (Figure 14c,d). Though it possessed much higher tensile ductility, the KAM value is much lower, and the strain distribution is more uniform in the sample tested at a higher strain rate of 10^{-2} s^{-1}. The variance of strain concentration along the heterogeneous grain structure interface can be attributed to the different deformation and strain accommodation behaviours under the applied testing conditions.

It is commonly accepted that stress concentration typically occurs in front of a planar array of dislocation pile up, which eventually leads to crack initiation. The continuous network of heterogeneous grain structure interface and the alignment of primary Al_6Mn particles along the columnar grain boundaries promoted the easy propagation of deformation cracks, leaving the columnar and equiaxed grain features on the fracture surface. Such failure behaviours have been reported in LPBF-fabricated AlSi10Mg alloys and Al-Ce-Mn alloys at room temperature, and the underlying failure mechanisms were attributed to the inherent microstructural and mechanical property heterogeneities [39,40]. Further, with the improvement of the tensile testing strain rate, the tensile fracture strain of the studied alloy was significantly improved. We suggest that the improved strain rate accelerated the dynamic recovery of dislocations through either dislocation interactions or grain boundary sinking, which effectively avoided severe dislocation pile-ups and the resultant stress concentrations during the later straining process. This can be reflected in the engineering stress-strain curves shown in Figure 8, where the strain hardening

effect was gradually reduced with the increment of strain rate. One exception is that the samples tested at 573 K exhibited an opposite strain hardening phenomenon, i.e., the strain hardening capability was enhanced with the increment of strain rate. This might be due to the significantly improved mobile dislocation density due to the easy activation of more dislocation sources under higher tensile temperatures, which balanced or even overcame dislocation recovery at higher strain rates. Overall, we propose the major intermediate temperature ductility dip mechanism in the studied Al-Mn-Sc alloy can be attributed to the microstructural and mechanical property heterogeneity of the generated grain structure at elevated temperatures.

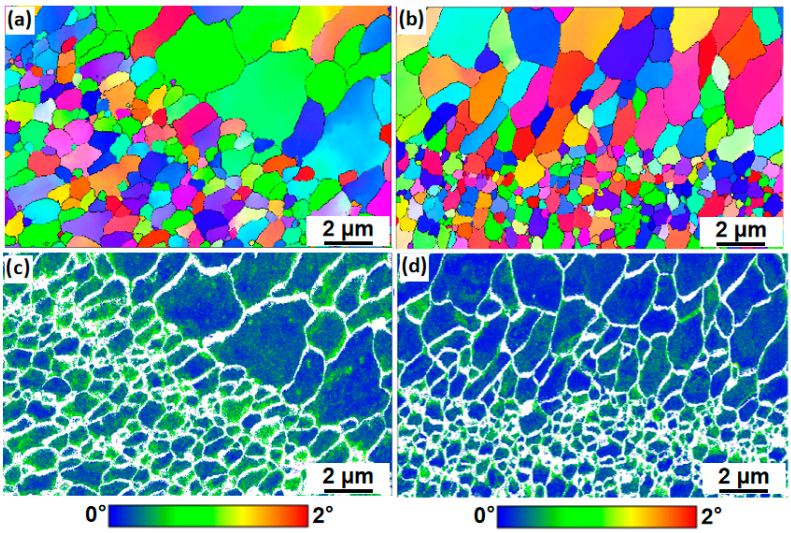

Figure 14. (**a**,**b**) EBSD images showing the heterogeneous grain structure interface and (**c**,**d**) the corresponding KAM mapping of strain distribution. The samples are tested at (**a**,**c**) 523 K, 10^{-4} s^{-1}, and (**b**,**d**) 523 K, 10^{-2} s^{-1}.

4.2.2. Yield Drop Behaviours

Similar to samples tested at room temperature, the engineering stress-strain curves also exhibited a yield drop behaviour at elevated temperatures under certain testing conditions. Specifically, the alloy showed obvious yield drops followed by a long stress plateau at 423 K and 523 K with different testing strain rates. At a given strain rate, the yield drop amplitude decreased significantly with the increment of tensile testing temperatures. The root cause of yield drop can be attributed to the formed heterogeneous grain structure of the studied alloy, especially the ultrafine equiaxed grains [41]. During the early plastic deformation stage, the initially generated dislocations are frequently absorbed along the ultrafine equiaxed grain boundaries due to the limited dislocation movement pathways. To maintain the bulk material deformation, higher tensile stress is normally required to activate more dislocation sources to yield the material, resulting in the so-called "extra hardening" phenomenon associated with higher yield strength [42]. In the meantime, the improved tensile stress also promoted higher dislocation density within the bulk material in the further deformation stage. According to the Johnston-Gilman (JG) model [43], the plastic strain rate $\dot{\varepsilon}$ can be generally written as

$$\dot{\varepsilon} \propto b\rho_m\tau \tag{2}$$

where b is the Burgers vector, ρ_m is the mobile dislocation density, and τ is the applied shear stress. At a given strain rate, the applied shear stress has to be decreased to balance the dramatic increment of the mobile dislocation density, which in turn causes the yield drop behaviour. After the yield drop, the dislocation density reaches a stationary value determined by the dynamic balance between dislocation multiplication and its annihila-

tion, resulting in a steady state engineering stress-strain curve as reflected by the long strain plateau.

The yield drop behaviour depends on the competition between dislocation generation and its dynamic recovery, which is significantly influenced by the applied tensile testing temperatures and strain rates. At a given strain rate, the dislocation activation sources in both columnar and equiaxed grain regions can be significantly increased with the increment of tensile testing temperatures, which in turn enhances the mobile dislocation density upon deformation. The dramatically increased dislocation density balanced the dislocation annihilation along fine grain boundaries at the initial deformation stage, which simultaneously weakened the yield drop behaviour. Further, at a certain testing temperature, the increased strain rate and the associated higher tensile stress enhanced the "extra hardening" phenomenon, leading to the more distinct yield drop phenomenon. It is worth noting though the generated Al_3(Sc, Zr) nanoprecipitates can impede the dislocation movement (before yielding) and contribute to alloy yield strength at elevated temperatures, further dislocations can then easily shear the precipitates after the first pass during plastic deformation, providing insignificant dislocation storage effects to contribute the work-hardening behaviour during the later plastic deformation process.

5. Conclusions

In this study, the microstructure and elevated temperature tensile behaviours of LPBF-fabricated Al-Mn-Sc alloy were studied. The effects of testing temperature and strain rate on the mechanical performance, as well as the underlying deformation mechanisms, were elucidated in detail. The following conclusions can be drawn:

(1) The LPBF-fabricated Al-Mn-Sc alloy demonstrated outstanding microstructural thermal stability, with no obvious grain recrystallisation, primary particle growth, and/or precipitate coarsening after tensile testing at elevated temperatures (423–573 K) and different strain rates (10^{-5}–10^{-2} s^{-1}).

(2) The Al-Mn-Sc alloy showed strain rate and temperature-dependent mechanical properties, with the yield strength decreasing with the increment of testing temperature and the decrement of the applied strain rate. The relationship between high-temperature yield strength, testing temperature and applied strain rate was established through a creep model.

(3) The alloy exhibited unusual ductility dip and distinct yield drop phenomenons under certain testing temperature and strain rate regimes. The different deformation and strain accommodation behaviours of the heterogeneous grain structure triggered the intermediate temperature embrittlement, while the "extra-hardening" phenomenon caused the yield drop.

Overall, the intermediate ductility dip and the yield drop phenomenons in the LPBF-fabricated Al-Mn-Sc alloy can be significantly influenced by the applied tensile testing temperatures and strain rates. Thus, the elevated temperature application of inoculates modified Al alloys with aforementioned heterogeneous grain structures is worth considering the material service environments, especially those under dynamic loading conditions. Moreover, the introduced inoculates in LPBF-processed Al alloys should also be further tailored for future high-performance, high-temperature Al alloy development.

Author Contributions: Methodology, data curation, validation, analysis, Y.Y.; data curation, investigation, C.L.; formal analysis, methodology, software, investigation, Z.C. and Y.Z.; funding acquisition, supervision, project administration, C.W.; conceptualisation, methodology, writing, funding acquisition, supervision, project administration, Q.J. All authors have read and agreed to the published version of the manuscript.

Funding: This research was funded by the National Natural Science Foundation of China (52201046, 52075354), the Natural Science Foundation of Jiangsu Province (No. BK20210727), the fellowship of China Postdoctoral Science Foundation (No. 2021M692337), and the Fundamental Research Program for Prospective Application of Suzhou City (No. SYG202126).

Data Availability Statement: The data presented in this study are all available in the paper.

Acknowledgments: The authors acknowledge the use of the facilities at the Analytical and Testing Center of Soochow University.

Conflicts of Interest: The authors declare that they have no known competing financial interests or personal relationships that could have appeared to influence the work reported in this paper.

References

1. Herzog, D.; Seyda, V.; Wycisk, E.; Emmelmann, C. Additive manufacturing of metals. *Acta Mater.* **2016**, *117*, 371–392. [CrossRef]
2. Popov, V.V.; Grilli, M.L.; Koptyug, A.; Jaworska, L.; Katz-Demyanetz, A.; Klob, D.; Balos, S.; Postolnyi, B.O.; Goel, S. Powder Bed Fusion Additive Manufacturing Using Critical Raw Materials: A Review. *Materials* **2021**, *14*, 909. [CrossRef] [PubMed]
3. Lewandowski, J.J.; Seififi, M. Metal additive manufacturing: A review of mechanical properties. *Annu. Rev. Mater. Res.* **2016**, *46*, 152–186. [CrossRef]
4. DebRoy, T.; Wei, H.L.; Zuback, J.S.; Mukherjee, T.; Elmer, J.W.; Milewski, J.O.; Beese, A.M.; Wilson-Heid, A.; De, A.; Zhang, W. Additive manufacturing of metallic components—Process, structure and properties. *Prog. Mater. Sci.* **2018**, *92*, 112–224. [CrossRef]
5. Wang, Y.M.; Voisin, T.; McKeown, J.T.; Ye, J.; Calta, N.P.; Li, Z.; Zeng, Z.; Zhang, Y.; Chen, W.; Roehling, T.T.; et al. Additively manufactured hierarchical stainless steels with high strength and ductility. *Nat. Mater.* **2018**, *17*, 63–70. [CrossRef] [PubMed]
6. Yap, C.Y.; Chua, C.K.; Dong, Z.L.; Liu, Z.H.; Zhang, D.Q.; Loh, L.E.; Sing, S.L. Review of selective laser melting: Materials and applications. *Appl. Phys. Rev.* **2015**, *2*, 041101. [CrossRef]
7. Fu, J.; Li, H.; Song, X.; Fu, M.W. Multi-scale defects in powder-based additively manufactured metals and alloys. *J. Mater. Sci. Technol.* **2022**, *122*, 165–199. [CrossRef]
8. Johnson, N.S.; Vulimiri, P.S.; To, A.C.; Zhang, X.; Brice, C.A.; Kappes, B.B.; Stebner, A.P. Machine learning for materials developments in metals additive manufacturing. *Addit. Manuf.* **2020**, *36*, 101641.
9. Tan, Q.; Liu, Y.; Fan, Z.; Zhang, J.; Yin, Y.; Zhang, M.X. Effect of processing parameters on the densification of an additively manufactured 2024 Al alloy. *J. Mater. Sci. Technol.* **2020**, *58*, 34–45. [CrossRef]
10. Xu, R.; Li, R.; Yuan, T.; Niu, P.; Wang, M.; Lin, Z. Microstructure metallurgical defects and hardness of Al-Cu-Mg-Li-Zr alloy additively manufactured by selective laser melting. *J. Alloys Compd.* **2020**, *835*, 155372. [CrossRef]
11. Li, G.; Li, X.; Guo, C.; Zhou, Y.; Tan, Q.; Qu, W.; Li, X.; Hu, X.; Zhang, M.X.; Zhu, Q. Investigation into the effect of energy density on densification, surface roughness and loss of alloying elements of 7075 aluminium alloy processed by laser powder bed fusion. *Opt. Laser Technol.* **2022**, *147*, 107621. [CrossRef]
12. Li, L.; Li, R.; Yuan, T.; Chen, C.; Wang, M.; Yuan, J.; Weng, Q. Microstructures and mechanical properties of Si and Zr modified Al-Zn-Mg-Cu alloy-A comparison between selective laser melting and spark plasma sintering. *J. Alloys Compd.* **2020**, *821*, 153520. [CrossRef]
13. Otani, Y.; Sasaki, S. Effects of the addition of silicon to 7075 aluminum alloy on microstructure, mechanical properties, and selective laser melting processability. *Mater. Sci. Eng. A* **2020**, *777*, 130079. [CrossRef]
14. Martin, A.; Vilanova, M.; Gil, E.; Sebastian, M.S.; Wang, C.Y.; Milenkovic, S.; Perez-Prado, M.T.; Cepeda-Jimenez, C.M. Influence of the Zr content on the processability of a high strength Al-Zn-Mg-Cu-Zr alloy by laser powder bed fusion. *Mater. Charact.* **2022**, *183*, 111650. [CrossRef]
15. Zhu, Y.; Zhao, Y.; Chen, B. A study on Sc- and Zr-modified Al–Mg alloys processed by selective laser melting. *Mater. Sci. Eng. A* **2022**, *833*, 142516. [CrossRef]
16. Lu, J.; Lin, X.; Kang, N.; Huang, W. Characterizations of micro-nano structure and tensile properties of a Sc modified Al-Mn alloy fabricated by selective laser melting. *Mater. Charact.* **2021**, *178*, 111305. [CrossRef]
17. Lu, J.; Lin, X.; Kang, N.; Cao, Y.; Wang, Q.; Li, J.; Zhang, L.; Huang, W. On the Sc induced solidification-heterogeneous microstructure in selective laser melted Al-5Mn alloys. *J. Mater. Process. Technol.* **2022**, *304*, 117562. [CrossRef]
18. Zhou, L.; Pan, H.; Hyer, H.; Park, S.; Bai, Y.; McWilliams, B.; Cho, K.; Sohn, Y. Microstructure and tensile property of a novel AlZnMgScZr alloy additively manufactured by gas atomization and laser powder bed fusion. *Scr. Mater.* **2019**, *158*, 24–28. [CrossRef]
19. Xue, N.; Liu, W.Q.; Zhu, L.; Muthuramalingam, T. Efect of Scandium in Al-Sc and Al-Sc-Zr Alloys Under Precipitation Strengthening Mechanism at 350 °C Aging. *Metals Mater. Inter.* **2021**, *27*, 5145–5153.
20. Jia, Q.; Rometsch, P.; Cao, S.; Zhang, K.; Huang, A.; Wu, X. Characterisation of AlScZr and AlErZr alloys processed by rapid laser melting. *Scr. Mater.* **2018**, *151*, 42–46. [CrossRef]
21. Li, R.; Chen, H.; Chen, C.; Zhu, H.B.; Wang, M.B.; Yuan, T.C.; Song, B. Selective Laser Melting of Gas Atomized Al-3.02Mg-0.2Sc-0.1Zr Alloy Powder: Microstructure and Mechanical Properties. *Adv. Eng. Mater.* **2019**, *21*, 1800650. [CrossRef]
22. Best, J.P.; Maeder, X.; Michler, J.; Spierings, A.B. Mechanical Anisotropy Investigated in the Complex SLM-Processed Sc-and Zr-Modified Al-Mg Alloy Microstructure. *Adv. Eng. Mater.* **2019**, *21*, 1801113. [CrossRef]
23. Li, R.; Wang, M.; Li, Z.; Cao, P.; Yuan, T.; Zhu, H. Developing a high-strength Al-Mg-Si-Sc-Zr alloy for selective laser melting: Crack-inhibiting and multiple strengthening mechanisms. *Acta Mater.* **2020**, *193*, 83–98. [CrossRef]
24. Jia, Q.; Rometsch, P.; Kürnsteiner, P.; Chao, Q.; Huang, A.; Weyland, M.; Bourgeois, L.; Wu, X. Selective laser melting of a high strength Al-Mn-Sc alloy: Alloy design and strengthening mechanisms. *Acta Mater.* **2019**, *171*, 108–118. [CrossRef]

25. Li, L.; Li, R.; Yuan, T.; Chen, C.; Zhang, Z.; Li, X. Microstructures and tensile properties of a selective laser melted Al-Zn-Mg-Cu (Al7075) alloy by Si and Zr microalloying. *Mater. Sci. Eng. A* **2020**, *787*, 139492. [CrossRef]
26. Wang, A.; Yan, Y.; Chen, Z.; Qi, H.; Yin, Y.; Wu, X.; Jia, Q. Characterisation of the multiple effects of Sc/Zr elements in selective laser melted Al alloy. *Mater. Charact.* **2022**, *183*, 111653. [CrossRef]
27. Jia, Q.; Rometsch, P.; Cao, S.; Zhang, K.; Wu, X. Towards a high strength aluminium alloy development methodology for selective laser melting. *Mater. Des.* **2019**, *174*, 107775. [CrossRef]
28. Spierings, A.B.; Dawson, K.; Heeling, T.; Uggowitzer, P.J.; Schäublin, R.; Palm, F.; Wegener, K. Microstructural features of Sc- and Zr-modified Al-Mg alloys processed by selective laser melting. *Mater. Des.* **2017**, *115*, 52–63. [CrossRef]
29. Griffiths, S.; Rossell, M.D.; Croteau, J.; Vo, N.Q.; Dunand, D.C.; Leinenbach, C. Effect of laser rescanning on the grain microstructure of a selective laser melted Al-Mg-Zr alloy. *Mater. Charact.* **2018**, *143*, 34–42. [CrossRef]
30. Vlach, M.; Stulikova, I.; Smola, B.; Kekule, T.; Kudrnova, H.; Danis, S.; Gemma, R.; Ocenasek, V.; Malek, J.; Tanprayoon, D.; et al. Precipitation in cold-rolled Al-Sc-Zr and Al-Mn-Sc-Zr alloys prepared by powder metallurgy. *Mater. Charact.* **2013**, *86*, 59–68. [CrossRef]
31. Abe, F.; Torsten-Ulf, K.; Viswanathan, R. *Creep-Resistant Steels*; Elsevier: Amsterdam, The Netherlands, 2008.
32. Chen, X.M.; Song, S.H.; Weng, L.Q.; Wang, K. A consideration of intergranular fracture caused by trace impurity sodium in an Al-5 wt.% Mg alloy. *Scr. Mater.* **2008**, *58*, 902–905. [CrossRef]
33. Pu, E.; Zheng, W.; Song, Z.; Zhang, K.; Liu, S.; Shen, W.; Dong, H. The effect of aging on the serrated yielding and intermediate temperature embrittlement of nickel-base C-276 alloy. *Mater. Sci. Eng. A* **2018**, *714*, 59–67. [CrossRef]
34. Németh, A.A.N.; Crudden, D.J.; Armstrong, D.E.J.; Collins, D.M.; Li, K.; Wilkinson, A.J.; Grovenor, C.R.M.; Reed, R.C. Environmentally-assisted grain boundary attack as a mechanism of embrittlement in a nickel-based superalloy. *Acta Mater.* **2017**, *126*, 361–371. [CrossRef]
35. Sun, Z.; Laitem, C.; Vincent, A. Dynamic embrittlement at intermediate temperature in a Cu-Ni-Si alloy. *Mater. Sci. Eng. A* **2008**, *477*, 145–152. [CrossRef]
36. Min, J.H.; Heo, Y.U.; Kwon, S.H.; Moon, S.W.; Kim, D.G.; Lee, J.S.; Yim, C.H. Embrittlement mechanism in a low-carbon steel at intermediate temperature. *Mater. Charact.* **2019**, *149*, 34–40. [CrossRef]
37. Pommier, H.; Busso, E.P.; Morgeneyer, T.F.; Pineau, A. Intergranular damage during stress relaxation in AISI 316L-type austenitic stainless steels: Effect of carbon, nitrogen and phosphorus contents. *Acta Mater.* **2016**, *103*, 893–908. [CrossRef]
38. Bahl, S.; Plotkowski, A.; Sisco, K.; Leonard, D.N.; Allard, L.F.; Michi, R.A.; Poplawsky, J.D.; Dehoff, R.; Shyam, A. Elevated temperature ductility dip in an additively manufactured Al-Cu-Ce alloy. *Acta Mater.* **2021**, *220*, 117285. [CrossRef]
39. Xiong, Z.H.; Liu, S.L.; Li, S.F.; Shi, Y.; Yang, Y.F.; Misra, R.D.K. Role of melt pool boundary condition in determining the mechanical properties of selective laser melting AlSi10Mg alloy. *Mater. Sci. Eng. A* **2019**, *740–741*, 148–156. [CrossRef]
40. Plotkowski, A.; Sisco, K.; Bahl, S.; Shyam, A.; Yang, Y.; Allard, L.; Nandwana, P.; Rossy, A.M.; Dehoff, R.R. Microstructure and properties of a high temperature Al-Ce-Mn alloy produced by additive manufacturing. *Acta Mater.* **2020**, *196*, 595–608. [CrossRef]
41. Wang, Z.; Lin, X.; Kang, N.; Hu, Y.; Chen, J.; Huang, W. Strength-ductility synergy of selective laser melted Al-Mg-Sc-Zr alloy with a heterogeneous grain structure. *Addit. Manuf.* **2020**, *34*, 101260. [CrossRef]
42. Khamsuk, S.; Park, N.; Gao, S.; Terada, D.; Adachi, H.; Tsuji, N. Mechanical properties of bulk ultrafine grained aluminum fabricated by torsion deformation at various temperatures and strain rates. *Mater. Trans.* **2014**, *55*, 106–113. [CrossRef]
43. Johnston, W.G.; Gilman, J.J. Dislocation velocities, dislocation densities, and plastic flow in lithium fluoride crystals. *J. Appl. Phys.* **1959**, *30*, 129–144. [CrossRef]

Disclaimer/Publisher's Note: The statements, opinions and data contained in all publications are solely those of the individual author(s) and contributor(s) and not of MDPI and/or the editor(s). MDPI and/or the editor(s) disclaim responsibility for any injury to people or property resulting from any ideas, methods, instructions or products referred to in the content.